

Fast, accurate, and predictive method for atom detection in site-resolved images of microtrap arrays

Marc Cheneau,* Romaric Journet, Matthieu Boffety, François Goudail, and Caroline Kulcsár
*Université Paris-Saclay, Institut d'Optique Graduate School,
CNRS, Laboratoire Charles Fabry, 91127, Palaiseau, France*

Pauline Trouvé-Peloux
DTIS, ONERA, Université Paris-Saclay, 91123, Palaiseau, France
(Dated: February 26, 2025)

We introduce a new method, rooted in estimation theory, to detect the individual atoms in site-resolved images of microtrap arrays, such as optical lattices or optical tweezers arrays. Using simulated images, we demonstrate a ten-fold reduction of the detection error rate compared to the popular method based on Wiener deconvolution, under a wide range of experimental conditions. The runtime is fully compatible with real-time applications, even for a very large arrays. Finally, we propose a rigorous definition for the signal-to-noise ratio of an image, and show that it can be used as a predictor for the detection error rate, which opens new prospect for the design of future experiments.

I. INTRODUCTION

Over the past 15 years, site-resolved imaging of atoms or molecules in arrays of optical microtraps, whether optical lattices or optical tweezers arrays, has been established as a sensitive probe of spatial correlations in a quantum many-body system [1, 2]. In a typical experimental setting, a two-dimensional array loaded with atoms, with an inter-site distance ranging from a few hundred nm to a few μm , is imaged onto a digital camera with a high-resolution objective. After calibration of the coordinates of the sites in the image and the profile of the point spread function (PSF) of the optical system, the image is then processed to detect the presence or absence of an atom in each site. The reconstruction of the site occupancies is therefore a classical estimation-detection problem [3, 4], where the signal to be estimated consists in the brightness of each site.

When the inter-sites distant is larger than the optical resolution, a simple binning approach is often sufficient to estimate the site brightnesses [5–8]. Otherwise, one has to resort to more elaborate estimation techniques. The methods employed so far can be broadly categorized as local non-linear least squares [9–12], local iterative algorithms [13, 14], deconvolution methods [15–22], local maximum likelihood estimation [23, 24] and supervised [25, 26] or unsupervised [27] neural networks. Recently, ref. [28] benchmarked several methods with a Cramér–Rao bound using labelled test images simulating an optical tweezers array experiment [28]. They showed that a non-linear least squares approach achieves a better accuracy than, for instance, the popular Wiener or Richardson–Lucy deconvolution, but at the cost of a prohibitive computation time.

In this article, we apply a generalized Wiener filter [3]—which uses the statistical properties of both the signal and the noise to provide an optimal linear estimate of the signal—to the reconstruction of the site occupancies. We focus on the more difficult problem posed by optical lattices, where neighboring sites often have a significant overlap, but the method equally applies to any type of microtrap array. Using labelled test images, we compare the performance of our method with that of the Wiener deconvolution, and demonstrate a ten-fold reduction of the detection error rate under a wide range of experimental conditions. Importantly, low computation times remain very low, well below 100 ms for 100×100 sites. We also keep the implementation simple by using the Python interpreted programming language and standard scientific computing libraries, and provide the reader with a tutorial example in the form of a Jupyter notebook [29].

Last but not least, this approach leads us to a rigorous definition of a signal-to-noise ratio for the reconstruction problem, i.e., a synthetic indicator of the intrinsic ‘difficulty’ of the estimation-detection problem under given experimental conditions. We show that this indicator can be used as a predictor for the detection error rate. This predictor should greatly improve the design of new experimental apparatuses because it allows one to establish clear specifications for the imaging system, rather than simply maximizing the optical resolution and the number of photons emitted by the atoms. One can then take advantage of the improved accuracy of our method to either lower the requirements on the imaging system, or reduce the inter-site distance to increase the coupling between sites and access new physics, for instance.

II. METHODOLOGY

To quantitatively evaluate and compare the performance of different reconstruction algorithms, we gener-

* marc.cheneau@institutoptique.fr

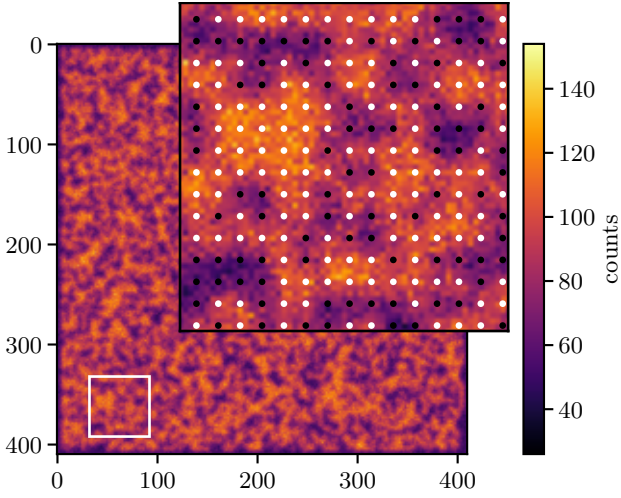


FIG. 1. **A randomly generated test image.** The image mimics an atomic gas loaded in an optical lattice. We chose the imaging parameters to make the reconstruction problem difficult, see Table I. The inset shows a zoom into the white square towards the bottom left corner of the image, with the white and black dots indicating, respectively, the occupied and empty sites. Our reconstruction method detects the atoms in this image with an error rate of 0.21 %, compared to 1.46 % with a deconvolution estimator, see Section IV

number of sites	N_s	100 × 100	
occupancy probability	p	0.6	
lattice spacing	a	4	pixel
PSF HWHM		3	pixel
brightness mean	μ	1 000	count / site
brightness variance	σ^2	100	count / site
background	k	50	count / pixel
readout noise variance	r^2	1	count / pixel

TABLE I. **Imaging parameters for Fig. 1.** The unit of length is the pixel size. An Airy disk with the same half width at half maximum (HWHM) as our Gaussian PSF would have its radius (first zero) at approximately $2.4 \times 3/4 \simeq 1.8 a$. With such a large radius, none of the usual resolution criteria is met.

ate random test images using an idealized model [30]. We define a square lattice with N_s sites in an image with N_p pixels, and denote a the lattice spacing in the image plane (measured in pixels). The top left site is centered on a pixel unless a global offset is applied to the site positions. We draw the occupancy of each site from a Bernoulli distribution with the occupancy probability p . We take the brightness of the empty sites to be zero, while that of the occupied site follows a normal distribution with its mean and variance denoted, respectively, by μ and σ^2 . Once the brightnesses have been chosen, we build a noiseless image by summing the PSF of each site multiplied by the corresponding brightness, and adding a uniform background k (we set the camera readout to zero for simplicity). We include the shot noise by treat-

ing each pixel of the noiseless image as the mean value of a Poisson distribution. We then add a normally distributed noise with zero mean and variance r^2 to account for the readout noise of a CMOS camera. In the following we designate the model parameters introduced above as the *imaging parameters*, since all but the occupancy probability characterize the imaging system or the imaging process.

The relationship between the site brightnesses and the pixel values in the test image can be summarized in the following matrix equation:

$$\mathbf{y} \sim \mathcal{P}(\mathbf{M}\mathbf{x} + \mathbf{k}) + \mathcal{N}(\mathbf{0}, \mathbf{r}^2). \quad (1)$$

Here, and in the following, small bold letters denote column vectors, capital bold letters matrices, and (small or capital) normal letters scalars. The vector \mathbf{y} represents the pixel values, \mathbf{x} the brightnesses, $\mathbf{k} = k\mathbf{1}$ the background, and $\mathbf{r}^2 = r^2\mathbf{1}$ the readout noise. \mathbf{M} is the measurement matrix, with $(\mathbf{M})_{ij}$ the integral over the i th pixel of the PSF centered on the j th site. $\mathcal{P}(\mathbf{u})$ and $\mathcal{N}(\mathbf{u}, \mathbf{v})$ denote, respectively, the multivariate Poisson distribution with mean \mathbf{u} , and for the multivariate normal distribution with mean \mathbf{u} and diagonal covariance matrix $\text{diag}(\mathbf{v})$. $\mathbf{1}$ and $\mathbf{0}$ denote the column vectors of ones and zeros.

We have chosen a Gaussian PSF for simplicity [31]; it is characterized by its half width at half maximum (HWHM), and normalized such that its area integral is equal to unity (i.e., $\sum_i (\mathbf{M})_{ij} = 1$). We truncate the PSF when the distance to the center is larger than 3 times the HWHM. The reader accustomed to modelling the PSF by an Airy disk can convert the Gaussian HWHM to the radius of the Airy disk by multiplying the former with a factor 2.4 (assuming that both functions have the same HWHM).

We show in Fig. 1 one example of a test image, mimicking an optical lattice configuration, which we will use throughout the article to illustrate our method. The corresponding imaging parameters, given in Table I, were chosen such that the reconstruction is barely possible using conventional techniques. In particular, the PSF HWHM is too large (with respect to a) for any of the usual resolution criteria to be met.

Denoting $\hat{\mathbf{x}}$ the estimated brightnesses (i.e., the output of an estimation algorithm), we quantify the estimation accuracy through the sum of squared residuals:

$$\text{SSR} \triangleq \|\hat{\mathbf{x}} - \mathbf{x}\|_2^2. \quad (2)$$

We label a site as occupied (empty) if its estimated brightness lies above (below) a global detection threshold. We quantify the detection accuracy through the detection error rate:

$$\text{DER} \triangleq \frac{\text{FP} + \text{FN}}{N_s}, \quad (3)$$

where FP and FN stand for the number of false positives and false negatives, and the terms ‘positives’ and

‘negatives’ refer to sites labelled as occupied or empty, respectively. Since we know the ground truth behind the test images, we simply choose the detection threshold which minimizes the DER.

III. OPTIMAL LINEAR ESTIMATOR

We now turn to the description of our approach to solve the estimation problem. It starts with the choice of a model for the relationship between the measurement (\mathbf{y}) and the signal (\mathbf{x}):

$$\mathbf{y} = \mathbf{M}\mathbf{x} + \mathbf{k} + \mathbf{n} . \quad (4)$$

Here, \mathbf{y} , \mathbf{x} , \mathbf{k} and \mathbf{M} have the same meaning as in Eq. (1). The vector \mathbf{n} accounts for the shot noise (originating from both the atomic and background signals) and for the camera readout noise. This model is relevant in most experimental contexts. It is even exact for our test images, because it is always possible to split a random vector with a Poisson statistics in its mean value (here, $\mathbf{M}\mathbf{x} + \mathbf{k}$) and uncorrelated fluctuations with zero mean value (here, \mathbf{n}). In the following we will always subtract the background from the image, and replace $\mathbf{y} + \mathbf{k}$ with \mathbf{y} for simplicity.

Ideally, the problem of estimating \mathbf{x} given \mathbf{y} should be treated in the maximum likelihood sense with an accurate statistical model for the brightness and the noise [32]. Given the bimodal nature of the probability distribution of the brightnesses (empty sites have zero brightness and occupied sites have a mean brightness $\mu > 0$), the resulting estimation algorithm would be non-linear, therefore time-consuming, and prone to fall into local minima.

To minimize the computation time and ensure the global convergence of the algorithm, we want to limit ourselves to linear estimators. The optimal linear estimator, also called generalized Wiener filter, is the matrix which minimizes the sum of squared errors between the estimated and true brightnesses:

$$\mathbf{H}_{\text{opt}} \triangleq \arg \min_{\mathbf{H}} [\text{SSE}(\mathbf{H})] , \quad (5)$$

with

$$\text{SSE}(\mathbf{H}) \triangleq \langle \|\hat{\mathbf{x}}(\mathbf{H}) - \mathbf{x}\|_2^2 \rangle , \quad (6)$$

and

$$\hat{\mathbf{x}}(\mathbf{H}) - \langle \mathbf{x} \rangle = \mathbf{H}(\mathbf{y} - \mathbf{M}\langle \mathbf{x} \rangle) . \quad (7)$$

In Eq. (6), \mathbf{x} and \mathbf{n} are treated as two sets of random variables, and $\langle \cdot \rangle$ denotes the expectation value over the probability distributions of \mathbf{x} and \mathbf{n} . The optimal estimator therefore provides the best estimates *on average* over all possible experimental outcomes, but not necessarily for all individual outcomes (we will come back to this point later). The reason for removing the expectation value of \mathbf{x} on both sides of Eq. (7) is to obtain a

sparse representation of the estimator, which greatly reduces the computation when dealing with large number of sites.

We show in Appendix A that the solution to Eq. (5) can be written in the form

$$\mathbf{H}_{\text{opt}} = (\mathbf{M}^\top \boldsymbol{\Sigma}_n^{-1} \mathbf{M} + \boldsymbol{\Sigma}_x^{-1})^{-1} \mathbf{M}^\top \boldsymbol{\Sigma}_n^{-1} , \quad (8)$$

where $\boldsymbol{\Sigma}_x \triangleq \langle (\mathbf{x} - \langle \mathbf{x} \rangle)(\mathbf{x} - \langle \mathbf{x} \rangle)^\top \rangle$ is the covariance matrix of the brightness and $\boldsymbol{\Sigma}_n \triangleq \langle \mathbf{n}\mathbf{n}^\top \rangle$ is the covariance matrix of the noise. In the following we will assume that both $\boldsymbol{\Sigma}_x$ and $\boldsymbol{\Sigma}_n$ are diagonal, which means that we neglect inter-site and inter-pixel correlations.

It is worth mentioning that the Wiener filter (8) can also be interpreted as the maximum a posteriori (MAP) estimator for a Gaussian prior, or as the solution of a weighted and regularized least-square problem. It involves only the first two moments of the probability distributions of \mathbf{x} and \mathbf{n} because it minimizes a quadratic loss function. While this is sufficient to capture most of the noise properties as soon as the mean count number is $\gg 1$, it clearly cannot account for the bimodal distribution of brightnesses. This limitation is common to all linear estimators, and the price to pay for a low runtime.

In principle, solving the inverse problem of Eq. (7) using Eq. (8) calls for the inversion of the matrix

$$\mathbf{A} \triangleq \mathbf{M}^\top \boldsymbol{\Sigma}_n^{-1} \mathbf{M} + \boldsymbol{\Sigma}_x^{-1} ; . \quad (9)$$

From a computational point of view, it is however much more efficient to solve the equivalent linear system

$$\mathbf{A}(\hat{\mathbf{x}} - \langle \mathbf{x} \rangle) = \mathbf{b} , \quad (10)$$

with

$$\mathbf{b} \triangleq \mathbf{M}^\top \boldsymbol{\Sigma}_n^{-1} (\mathbf{y} - \mathbf{M}\langle \mathbf{x} \rangle) . \quad (11)$$

Since \mathbf{A} is positive-definite by construction, and sparse because only nearby sites have overlapping PSFs, we naturally choose a sparse conjugate-gradient solver [33] for this task.

IV. TWO-STEP ESTIMATION

The expression (8) of the optimal linear estimator explicitly involves the covariance matrices $\boldsymbol{\Sigma}_x$ and $\boldsymbol{\Sigma}_n$, which are usually not available experimentally. One therefore needs some strategy to infer their value from the measured image itself. We propose to do this in two steps, which we briefly describe in this section. The reader can refer to Appendix B for more details and justifications.

First, we assume that all sites have the same brightness distribution, and that all pixels have the same noise distribution. We then determine $\langle \mathbf{x} \rangle$ from the total number of counts in the image, and treat the ratio $\boldsymbol{\Sigma}_n / \boldsymbol{\Sigma}_x$ as a free parameter, which we determine by maximizing

the Fisher linear discriminant (i.e. the contrast) of the bimodal distribution of estimated brightnesses.

In the second step, we consider that each site has its own occupancy probability, reflecting the prior information contained in the image: the sites which appear brighter in the image are probably occupied, while those which appear darker are probably empty. We introduce the occupancy probability vector \mathbf{p} , and determine \mathbf{p} , μ and σ by maximizing their likelihood given the estimate obtained in the first step. Finally, we compute $\langle \mathbf{x} \rangle$, Σ_x and Σ_n by applying Eqs. (14) to (16) to each site i , with p replaced by $(\mathbf{p})_i$. The second step will be more accurate than the first because all the sites with $(\mathbf{p})_i \simeq 0$ will have their estimated brightness tied to 0, and all those with $(\mathbf{p})_i \simeq 1$ will have their estimated brightness tied to μ (up to $\sim \sigma$); The number of parameters to be determined will therefore be reduced.

We apply this two-step procedure to the test image in Fig. 1 for illustration. In Fig. 2, we compare the histograms of the true brightnesses (top panel), and of the estimated brightnesses obtained after the 1st and 2nd steps (middle and bottom panels, respectively). The histogram of the first estimate follows a Gaussian mixture, which is to be expected since the SSE is a quadratic loss function. The measured DER is 0.85% in this case (threshold at $\simeq 476$), which quantitatively matches the value computed by integrating the tails of the Gaussian modes on both side of the threshold. The histogram of the second estimate looks much closer to the true histogram, with most brightnesses localized around 0 or μ , and only few values in-between. As a result, the measured DER is much lower: only 0.21% (threshold at $\simeq 432$). For comparison, a linear estimator based on the popular Wiener deconvolution filter (see Section VI) gives a DER of 1.46%.

In the following, we refer to the 1st and 2nd estimates, respectively, as the *globally optimal* and *locally optimal* estimates, to emphasize the different point of view adopted in the two cases.

V. SIGNAL-TO-NOISE RATIO

A valuable by-product of our approach is the possibility to rigorously define a signal-to-noise ratio for the estimation problem, namely

$$\text{SNR} \triangleq 10 \log_{10} \left(\frac{N_s \mu^2}{\text{SSE}(\mathbf{H}_{\text{opt}})} \right). \quad (12)$$

When the imaging parameters are known, the SNR can be explicitly computed using the following identity, derived in Appendix A:

$$\text{SSE}(\mathbf{H}_{\text{opt}}) = \text{trace}[(\mathbf{I} - \mathbf{H}_{\text{opt}} \mathbf{M}) \Sigma_x], \quad (13)$$

where \mathbf{I} is the identity matrix.

As an illustration, let us consider a test image like the one displayed in Fig. 1. Since all sites have the same

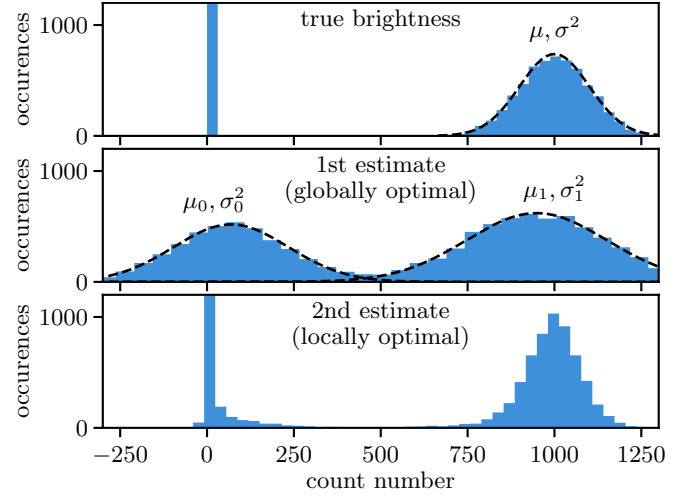


FIG. 2. **Two-step estimation.** Each panel represents a histogram of the brightnesses corresponding the test image in Fig. 1. Top panel: true brightnesses; Middle panel: first estimate (globally optimal); Bottom panel: second estimate (locally optimal). The dashed line in the top panel represents the Gaussian brightness distribution of the occupied sites, whose mean μ and variance σ^2 are given in Table I. The dashed lines in the middle panel show the two modes of the most likely Gaussian mixture distribution, with means $\mu_{0/1}$ and variances $\sigma_{0/1}^2$.

brightness distribution and all pixels have the same noise distribution, we can write $\langle \mathbf{x} \rangle = \langle x \rangle \mathbf{1}$, $\Sigma_x = \Sigma_x \mathbf{I}$ and $\Sigma_n = \Sigma_n \mathbf{I}$, with

$$\langle x \rangle = p\mu, \quad (14)$$

$$\Sigma_x = p(1-p)\mu^2 + p\sigma^2, \quad (15)$$

$$\Sigma_n = \frac{p\mu}{N_p} (\mathbf{1}^T \mathbf{M} \mathbf{1}) + k + r^2. \quad (16)$$

With the imaging parameters from Table I, we obtain a SNR of 14.8 dB [34]. As shown in Section VI, the strength of our definition of the SNR is that it synthesizes all system parameters into a single number, which determines the detection error rate. For instance, we obtain almost the same SNR (14.9 dB) if we simultaneously scale up the PSF HWHM from $3a/4$ to a , and multiply both μ and σ by a factor 10, while keeping all other parameters constant. We reach identical detection error rates of, respectively, $0.9 \pm 0.1\%$ and $0.2 \pm 0.1\%$ for the globally and locally optimal estimators, compared to $1.4 \pm 0.1\%$ with a standard deconvolution method. Here, the uncertainties correspond to the standard deviation over 50 random test images for each parameter set.

It would be handy of course to have a simpler expression than Eq. (12) to evaluate the SNR, with the individual imaging parameters appearing explicitly. Unfortunately, we can only obtain such expression in the trivial limit where there is no overlap between the PSFs, i.e., $\mathbf{M}^T \mathbf{M} = \mathbf{I}$. In this case, Eq. (12) reduces to $\text{SNR} \sim 10 \log_{10}[\mu^2(\Sigma_x^{-1} + \Sigma_n^{-1})]$, which means that the signal

power is given by the squared brightness mean, and the noise power by (half) the harmonic mean of the brightness and noise variances. We warn the reader, however, that this simple expression must be used very cautiously, as it completely ignores the crucial role played by the PSF overlap. With the parameters of Table I, for instance, it predicts a SNR of about 40 dB, which is 25 dB larger than the correct SNR.

VI. BENCHMARKING

We now compare the performance of the optimal estimator, both in its global and local versions, against a linear estimator based on the popular Wiener deconvolution filter. The implementation of the deconvolution estimator is presented in detail in Appendix C.

A. Accuracy

To begin with, we generate hundreds of test images with random imaging parameters, covering a wide range of experimental conditions and SNR, see Table II. We process each image successively with the globally optimal, locally optimal, and deconvolution estimators [35], and compute the estimation and detection accuracies, according to Eqs. (2) and (3). The results are plotted in Fig. 3 as a function of the SNR. We draw two conclusions from these graphs. First, the optimal linear estimator, both in its globally or locally optimal version, systematically outperforms the deconvolution estimator. The gain in accuracy is important with the locally optimal estimator, with a reduction of the DER by a factor ten when the SNR is above 15 dB, i.e. under typical experimental conditions.

Fig. 3 also confirms the relevance of our definition of the SNR as a synthetic indicator of the intrinsic ‘difficulty’ of the estimation problem, since the measured SSR collapse onto a single curve for each estimator. When considering the DER, one can expect that the ratio σ/μ also plays a role as it sets a lower bound on the DER that can be reached at infinite SNR. This effect should however be negligible as soon as σ is a few times smaller than μ .

B. Runtime

Another important aspect to take into consideration when comparing different estimators is their computation time. In Fig. 4, we show the runtimes (wall-clock times) of the globally optimal, locally optimal, and deconvolution estimators for the imaging parameters in Table I and an increasing number of sites. The runtime of the locally optimal estimator is the time it takes to run both steps of estimation, not just the second step. While the deconvolution method is always faster, the runtime

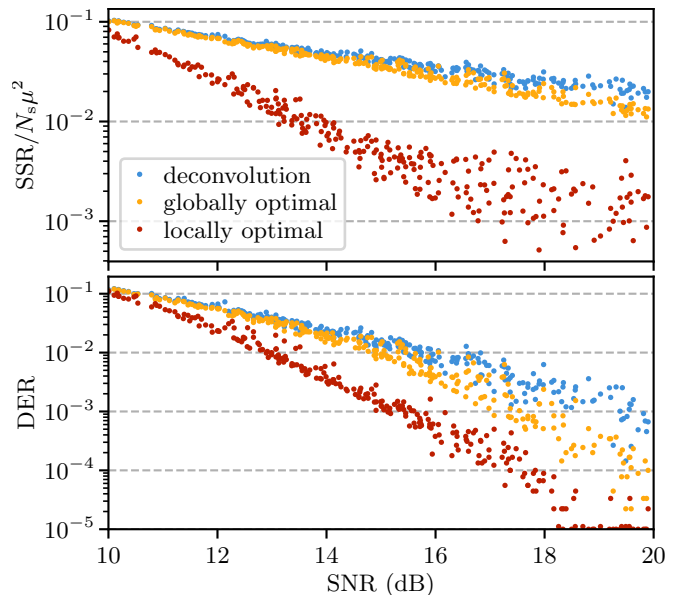


FIG. 3. **Accuracy vs. SNR.** We generate test images with random imaging parameters (given in Table II), and analyze them successively with an estimator based on the Wiener deconvolution filter (blue dots), and with the globally and locally optimal linear estimators (yellow and red dots, respectively). We have sorted the images by their signal-to-noise ratio (SNR, see Eq. (12)). The top panel shows the normalized sum of squared residuals (SSR, see Eq. (2)). The bottom panel shows the detection error rate (DER, see Eq. (3)). A floor value of 10^{-5} was set for the DER so that each point is visible.

number of sites	N_s	300×300	
occupancy probability	p	$[0.2, 0.8]$	
lattice spacing	a	$[1.5, 5]$	pixel
PSF HWHM		$[0.5, 1] \times a$	pixel
brightness mean	μ	$[100, 10\,000]$	count / site
brightness variance	σ^2	$(\mu/10)^2$	count / site
background	k	$[10, 1\,000]$	count / pixel

TABLE II. **Imaging parameters for Fig. 3.** The intervals give the boundaries of the uniform distributions from which we have drawn the imaging parameters. The PSF HWHM is defined as a random fraction of the lattice period. We take the brightness variance to be 10% of the brightness mean. The parameters which do not appear in this table have the same value as in Table I. We have increased the number of sites compared to Table I in order to more measure the DER with a higher precision.

of the optimal estimator remains well below 100 ms for a number of sites as large as 10^4 , which makes it perfectly suitable for real-time usage in all existing experiments. Note that the runtime of the deconvolution estimator depends on both N_s and N_p , whereas that of the optimal estimator only depends on N_s . More details on the runtime measurement are given in Appendix D.

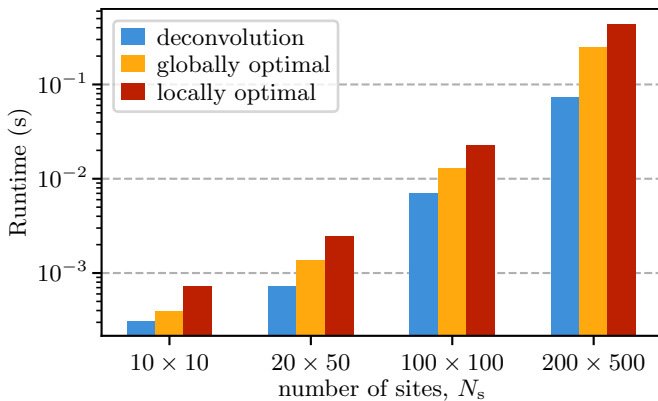


FIG. 4. **Runtime.** The runtime corresponds to the computation of an estimate for an image generated with the imaging parameters in Table I (except for the varying number of sites). The runtime of the locally optimal estimator is the time it takes to run both steps successively, not just the second step.

C. Robustness against calibration errors

All estimators used or proposed so far for the reconstruction of the site occupancy assume that the site coordinates and the PSF have been correctly calibrated beforehand. In this last section, we study how robust the optimal and deconvolution estimators are against two possible calibration errors: an error in the lattice position (or phase) and an error in the PSF HWHM. By error, we mean that the value of the parameter used to build the measurement matrix in Eq. (8) is not equal to the value of the parameter which was used to generate the test image. For a given calibration error, we then computed \hat{x} using the optimal and deconvolution estimators. We display the results in Fig. 5, with the left and right columns showing the effect of an error in the lattice position and in the PSF HWHM, and the top and bottom rows showing the normalized SSR and the DER, respectively. We see that the optimal estimator has a sensitivity to these calibration errors which is comparable to that of the deconvolution estimator, and should therefore perform well under realistic experimental conditions.

VII. CONCLUSION

We have applied a generalized Wiener filter to the atom detection in site-resolved fluorescence images of arrays of optical microtraps. We have obtained superior results over the standard method based on Wiener deconvolution, while keeping a low computation time, compatible with real-time applications. The same conclusion should hold for any other linear method, including Richardson-Lucy deconvolution, or ordinary least squares [36].

Our method is robust against calibration errors, and offers the possibility (not illustrated in this article) to account for spatial inhomogeneities in the distribution

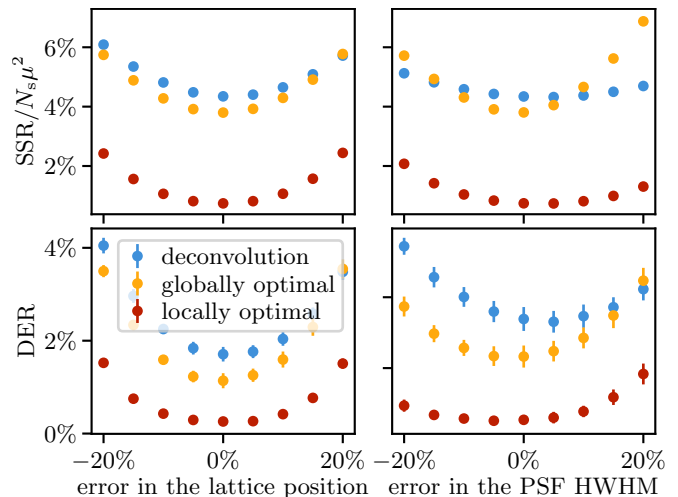


FIG. 5. **Robustness against calibration errors.** Each point is an average over 10 test images generated with the imaging parameters of Table I. We use the same set of test images for each value of the errors in the lattice positions and PSF HWHM. The error bars represent the standard deviation over the test images; they are sometimes too small to be visible. We give the errors in the lattice position as a percentage of the lattice period a , and the errors in the PSF HWHM as a percentage of the true value.

of atoms, readout noise, or PSF. For instance, one can easily disregard hot pixels by removing the corresponding lines in the measurement matrix. We are therefore convinced that it will keep its accuracy under real experimental conditions.

Benchmarking against supervised or unsupervised machine learning approaches remains to be done. Since our method includes the statistics of the signal and the noise up to the second order moments, it should be competitive with these methods. Of, course, the fact that we can optimize the few free parameters of our estimator from a single image, or just a few images, is a clear asset.

Finally, the Wiener filter theory also lead us to a rigorous definition of a signal-to-noise ratio for the estimation problem. This opens prospect for a more efficient design of future experiments, by taking into account simultaneously the performance of the imaging systems, the expected amount of signal and desired inter-site distance.

ACKNOWLEDGMENTS

The authors thank Félix Faisant, Thomas Chalopin, David Clément for their critical reading of the manuscript, and Anaïs Molineri for early work on the problem treated here.

Appendix A: Optimal linear estimator

In this section we explain how we have derived the expression (8) of the optimal linear estimator. We take $\langle \mathbf{x} \rangle = \mathbf{0}$ for simplicity. We start by writing the squared norm as the trace of the outer product and expand all terms:

$$\text{SSE}(\mathbf{H}) = \langle \text{trace}[(\mathbf{H}\mathbf{y} - \mathbf{x})(\mathbf{H}\mathbf{y} - \mathbf{x})^\top] \rangle \quad (\text{A1})$$

$$= \text{trace}[\mathbf{H}\langle \mathbf{y}\mathbf{y}^\top \rangle \mathbf{H}^\top - \mathbf{H}\langle \mathbf{y}\mathbf{x}^\top \rangle - \langle \mathbf{x}\mathbf{y}^\top \rangle \mathbf{H}^\top + \langle \mathbf{x}\mathbf{x}^\top \rangle] . \quad (\text{A2})$$

The optimal estimator is such that the derivative of the SSE with respect to \mathbf{H} is identically zero, which gives [37, Eqs. (100), (104) and (111)]:

$$\left. \frac{\text{dSSE}}{\text{d}\mathbf{H}} \right|_{\mathbf{H}_{\text{opt}}} = 2[\mathbf{H}_{\text{opt}}\langle \mathbf{y}\mathbf{y}^\top \rangle - \langle \mathbf{x}\mathbf{y}^\top \rangle] = \mathbf{0} , \quad (\text{A3})$$

hence

$$\mathbf{H}_{\text{opt}} = \langle \mathbf{x}\mathbf{y}^\top \rangle (\langle \mathbf{y}\mathbf{y}^\top \rangle)^{-1} . \quad (\text{A4})$$

We proceed further by replacing the image vector \mathbf{y} with $\mathbf{M}\mathbf{x} + \mathbf{n}$:

$$\langle \mathbf{y}\mathbf{x}^\top \rangle = \langle (\mathbf{M}\mathbf{x} + \mathbf{n})\mathbf{x}^\top \rangle \quad (\text{A5})$$

$$= \mathbf{M}\langle \mathbf{x}\mathbf{x}^\top \rangle , \quad (\text{A6})$$

and

$$\langle \mathbf{y}\mathbf{y}^\top \rangle = \langle (\mathbf{M}\mathbf{x} + \mathbf{n})(\mathbf{M}\mathbf{x} + \mathbf{n})^\top \rangle \quad (\text{A7})$$

$$= \mathbf{M}\langle \mathbf{x}\mathbf{x}^\top \rangle \mathbf{M}^\top + \langle \mathbf{n}\mathbf{n}^\top \rangle , \quad (\text{A8})$$

In deriving these results, we have used the noise properties $\langle \mathbf{x}\mathbf{n}^\top \rangle = \langle \mathbf{x} \rangle \langle \mathbf{n}^\top \rangle$ (\mathbf{x} and \mathbf{n} are uncorrelated), and $\langle \mathbf{n} \rangle = \mathbf{0}$.

The matrices $\langle \mathbf{x}\mathbf{x}^\top \rangle$ and $\langle \mathbf{n}\mathbf{n}^\top \rangle$ are the covariance matrices of \mathbf{x} and \mathbf{n} , denoted Σ_x and Σ_n in the main text. Combining Eqs. (A4), (A6) and (A8) gives

$$\mathbf{H}_{\text{opt}} = \Sigma_x \mathbf{M}^\top (\mathbf{M} \Sigma_x \mathbf{M}^\top + \Sigma_n)^{-1} . \quad (\text{A9})$$

This expression turns out to be inconvenient for efficiently computing the solution to the problem. We obtain the more useful expression in Eq. (8) by applying the so-called Woodbury identity [37, Eq. (158)] (which holds because Σ_x and Σ_n are both positive definite by definition).

Finally, we can also compute the SSE corresponding to the optimal estimator by combining Eqs. (A2), (A6), (A8) and (A9):

$$\begin{aligned} \text{SSE}(\mathbf{H}_{\text{opt}}) &= \text{trace}[\mathbf{H}_{\text{opt}}(\mathbf{M}\Sigma_x\mathbf{M}^\top + \Sigma_n)\mathbf{H}_{\text{opt}}^\top \\ &\quad - \mathbf{H}_{\text{opt}}\mathbf{M}\Sigma_x - \Sigma_x\mathbf{M}^\top\mathbf{H}_{\text{opt}}^\top + \Sigma_x] \end{aligned} \quad (\text{A10})$$

$$= \text{trace}[(\mathbf{I} - \mathbf{H}_{\text{opt}}\mathbf{M})\Sigma_x] . \quad (\text{A11})$$

Appendix B: Two-step estimation

The optimal linear estimator depends on the statistical properties of \mathbf{x} and \mathbf{n} through their covariance matrices, Σ_x and Σ_n . It must be applied to a zero-mean image, which requires the knowledge of the expectation value $\langle \mathbf{x} \rangle$. Since these parameters are usually not known before the image is processed, we need a strategy to infer their value from the image itself. This can be done in two steps, which we describe in this section.

1. First step (globally optimal)

In the first step, we write $\langle \mathbf{x} \rangle = \langle x \rangle \mathbf{1}$, $\Sigma_x = \Sigma_x \mathbf{I}$, and $\Sigma_n = \Sigma_n \mathbf{I}$. This means that we assume uniform brightness and noise distributions, and neglect all inter-site or inter-pixel correlations. We can then rewrite the optimal linear estimator in the form

$$\mathbf{H}_{\text{opt}} = \left(\mathbf{M}^\top \mathbf{M} + \frac{\Sigma_n}{\Sigma_x} \mathbf{I} \right)^{-1} \mathbf{M}^\top . \quad (\text{B1})$$

Here, the ratio Σ_n/Σ_x acts as a regularization for the inverse of the Gram matrix $\mathbf{M}^\top \mathbf{M}$. It is of particular importance when the PSF of neighboring sites significantly overlap, and the inverse of the Gram matrix is ill-conditioned.

The mean brightness $\langle x \rangle$ is very easily determined in this case, since it is equal to the sum of all pixel values, divided by the number of sites in the image:

$$\langle x \rangle = \frac{1}{N_s} \sum_i (\mathbf{y})_i . \quad (\text{B2})$$

The regularization parameter Σ_n/Σ_x will be treated as a free parameter, which we call the *regularization parameter*, leading to the parameterized estimator

$$\mathbf{H}(\gamma) = (\mathbf{M}^\top \mathbf{M} + \gamma \mathbf{I})^{-1} \mathbf{M}^\top . \quad (\text{B3})$$

The effect of γ is illustrated in the top panel of Fig. 6. A weak regularization will make the solution extremely sensitive to the noise, leading to a large spread of the estimated brightness distribution. On the contrary, a strong regularization will make the solution insensitive to noise, but will localize it around $\langle x \rangle$. In both cases, the estimate is inaccurate, and the contrast between the two modes of the distribution is weak. On the contrary, the optimal regularization $\gamma_{\text{opt}} \triangleq \Sigma_n/\Sigma_x$ will result in an accurate estimation and a well contrasted distribution. To quantify this behavior, we have applied the parameterized estimator $\mathbf{H}(\gamma)$ to test images generated using the parameters of Table I, and plotted the normalized SSR of the estimates against γ , see the middle panel of Fig. 6. It is clear that the most accurate estimate corresponds to $\gamma = \gamma_{\text{opt}}$.

Of course, one cannot compute the SSR in a real experiment since the true \mathbf{x} is not known. As an alternative,

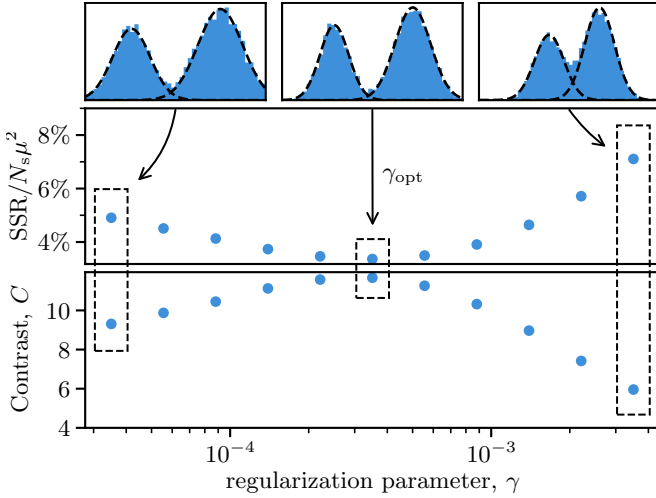


FIG. 6. **Optimization of the regularization parameter in the first step.** The parameterized estimator $\mathbf{H}(\gamma)$ is applied to the test image in Fig. 1. Top panel: estimated brightness distribution for $\gamma = \gamma_{\text{opt}}/10$ (left), $\gamma = \gamma_{\text{opt}}$ (middle), and $\gamma = 10\gamma_{\text{opt}}$ (right), with $\gamma_{\text{opt}} \triangleq \Sigma_n/\Sigma_x$. The dashed lines are the most likely normal distributions associated with each mode of the bimodal distribution. Middle panel: normalized SSR vs. γ . Bottom panel: contrast of the estimated brightness distribution vs. γ .

we propose to optimize γ by maximizing the contrast of the bimodal distribution of $\hat{\mathbf{x}}$. To define this contrast, we start by modeling the distribution of estimated brightnesses obtained with $\mathbf{H}(\gamma)$ with a Gaussian mixture distribution:

$$\pi(\hat{x}) = (1-p)\mathcal{N}(\hat{x}; \mu_0, \sigma_0) + p\mathcal{N}(\hat{x}; \mu_1, \sigma_1), \quad (\text{B4})$$

where $\mathcal{N}(x; \mu, \sigma)$ is the normal distribution with mean μ and variance σ^2 evaluated at x , and the labels ‘0’ and ‘1’ refer to the empty and occupied modes, respectively. We determine the parameters p , $\mu_{0/1}$ and $\sigma_{0/1}$ by maximizing the likelihood function for $\hat{\mathbf{x}}$, using the expectation-maximization algorithm implemented in the `mixture.GaussianMixture` class from the scikit-learn Python library [38]. A standard definition of the contrast for such distribution is the Fisher linear discriminant:

$$C = \frac{(\mu_1 - \mu_0)^2}{\sigma_1^2 + \sigma_0^2}. \quad (\text{B5})$$

The bottom panel of Fig. 6 shows how this contrast varies with γ . As expected, it reaches a maximum exactly where the SSR reaches a minimum, i.e., for $\gamma = \gamma_{\text{opt}}$.

The optimization procedure described above relies on the fact that the number of sites is large enough to provide a good representation of the distribution of estimated brightnesses. If this is not the case with a single image, it may be necessary to treat simultaneously several images obtained under the same experimental conditions.

2. Second step (locally optimal)

As illustrated in Fig. 3, the estimate obtained in the first step is only slightly more accurate than that obtained with the Wiener deconvolution. We can improve the estimate a lot, however, if we realize that the image contains information on the distribution of site brightnesses that was not used before: the sites which appear brighter in the image are probably occupied, while those which appear darker are probably empty. Following this line of thought means that we now regard the expectation values in Eqs. (6) and (7) as *conditional* on the image.

Let us formalize this idea. We still assume that all occupied sites have the same brightness mean and variance, denoted μ and σ^2 , but we now allow each site to have its own occupancy probability. We gather these occupancy probabilities in the vector \mathbf{p} . Within this new model, the covariance matrix of the noise vector is given by

$$\Sigma_n = \text{diag}(\mathbf{H}\mathbf{x} + \mathbf{k} + \mathbf{r}^2), \quad (\text{B6})$$

and the mean value and covariance matrix of the brightness vector by

$$\langle \mathbf{x} \rangle = \mathbf{p}\mu, \quad (\text{B7})$$

$$\Sigma_x = \text{diag}[\mathbf{p}(1-\mathbf{p})\mu^2 + \mathbf{p}\sigma^2]. \quad (\text{B8})$$

Here, the product between two vectors is element-wise.

To quantify how bright or dark appears in the image, we rely on the $\hat{\mathbf{x}}$ obtained after the first step. We then set the occupancy probability of the i th site to

$$(\mathbf{p})_i = \frac{p\mathcal{N}[(\hat{\mathbf{x}})_i; \mu_1, \sigma_1]}{(1-p)\mathcal{N}[(\hat{\mathbf{x}})_i; \mu_0, \sigma_0] + p\mathcal{N}[(\hat{\mathbf{x}})_i; \mu_1, \sigma_1]}, \quad (\text{B9})$$

where the Gaussian mixture parameters p , $\mu_{0/1}$ and $\sigma_{0/1}$ are those from the first step.

Once we have estimated the occupancy probability vector \mathbf{p} , we can directly apply Eq. (B6) to compute the covariance matrix of the noise vector. For the mean and covariance matrix of the brightness vector, there is one more step to go before applying Eqs. (B7) and (B8), which is to determine the parameters μ and σ^2 . This is done using the identities

$$p\mu = \frac{1}{N_s} \sum_i (\mathbf{y})_i, \quad (\text{B10})$$

and

$$\sigma_1^2 = \sigma^2 + \sigma_0^2. \quad (\text{B11})$$

The first identity corresponds to Eq. (B2), and uses the fact that the optimal linear estimator is unbiased (the mean value is conserved). The second identity expresses the fact that: 1. the variance of the brightness in the occupied mode (σ_1^2) combines the variance of the true brightness (σ^2) and the estimation errors; 2. the estimation error can be identified with the variance of the empty mode (σ_0^2) since the brightness of empty sites is identically zero.

Appendix C: Deconvolution estimator

The deconvolution estimator against which we benchmark our optimal linear estimator uses the Wiener deconvolution filter. This filter multiplies each two-dimensional spatial frequency (f_i, f_j) in the image by

$$G(f_i, f_j) = \frac{\tilde{C}(f_i, f_j)}{|\tilde{C}(f_i, f_j)|^2 + \lambda}, \quad (\text{C1})$$

where \tilde{C} is the Fourier transform of the PSF (which is assumed to be uniform across the image), and λ is a free parameter. The filtered image is then given by

$$\mathbf{y}^* = \mathbf{F}^\dagger \mathbf{G} \mathbf{F} (\mathbf{y} - \bar{\mathbf{y}}), \quad (\text{C2})$$

where \mathbf{F} denotes the unitary Fourier matrix, \mathbf{G} is the diagonal matrix constructed from Eq. (C1), and $\bar{\mathbf{y}} = \bar{y}\mathbf{1}$ is the average of the pixel values in the input image. In practice, we use the `restoration.wiener` function from the `scikit-image` Python library [39].

To extract the site brightnesses from the filtered image, we first convolve \mathbf{y}^* by a disk-shaped kernel of radius $d \in \mathbb{R}$, i.e., a matrix of size $(2\lceil d \rceil + 1) \times (2\lceil d \rceil + 1)$ with all entries within a distance d to the center equal to 1, and all others to 0. Then, we compute the linear interpolation of the result at the site coordinates. Since the Wiener deconvolution filter, the convolution, and the linear estimation can all be cast in matrix form, the deconvolution estimator as a whole is a linear estimator. These last

two steps are performed using the `ndimage.convolve` and `ndimage.map_coordinates` functions from the Scipy library [40].

For each test image, we have performed a joint optimization of the tuning parameters λ and d by maximizing the contrast of the estimated brightness distribution (as defined in Appendix B). Since the process described above is not guaranteed to preserve the absolute brightness of each site, we further applied an affine transformation to the estimated brightness values before computing the SSR for Fig. 3. The parameters of the affine transformation are optimized by minimizing the resulting SSR.

Appendix D: Runtime

The numerical implementation is in Python, uses mainly the standard libraries NumPy [41] and SciPy [40], and runs on a standard desktop computer (Intel Core i9-10900K CPU with the Intel MKL library).

We measure the runtime using the `%timeit` magic command from IPython, keeping the default settings. We exclude all the steps which precede the computation of the final estimate, like the optimization of the free parameters, or the computation of the matrices \mathbf{M} and $\mathbf{M}^\dagger \mathbf{M}$. This is a meaningful choice because these quantities need not be determined for every single image.

The sparse conjugate-gradient solver is a slightly optimized version of the SciPy `sparse.linalg.cg` function, and includes a Jacobi (or diagonal) preconditioner [42]. We have set its convergence check to 10^{-4} .

-
- [1] C. Gross and W. S. Bakr, *Nature Physics* **17**, 1316 (2021).
 - [2] A. M. Kaufman and K.-K. Ni, *Nature Physics* **17**, 1324 (2021).
 - [3] S. M. Kay, *Fundamentals of statistical signal processing, Vol. I: Estimation Theory* (Prentice-Hall, 1993).
 - [4] S. M. Kay, *Fundamentals of statistical signal processing, vol. II: Detection theory* (Prentice-Hall, 1998).
 - [5] M. Kwon, M. F. Ebert, T. G. Walker, and M. Saffman, *Physical Review Letters* **119**, 180504.
 - [6] M. A. Norcia, A. W. Young, and A. M. Kaufman, *Physical Review X* **8**, 041054 (2018).
 - [7] A. Cooper, J. P. Covey, I. S. Madjarov, S. G. Porsev, M. S. Safronova, and M. Endres, *Physical Review X* **8**, 041055 (2018).
 - [8] I. S. Madjarov, Entangling, controlling, and detecting individual strontium atoms in optical tweezer arrays (2021).
 - [9] W. S. Bakr, J. I. Gillen, A. Peng, S. Folling, and M. Greiner, *Nature* **462**, 74 (2009).
 - [10] M. F. Parsons, F. Huber, A. Mazurenko, C. S. Chiu, W. Setiawan, K. Wooley-Brown, S. Blatt, and M. Greiner, *Physical Review Letters* **114**, 213002 (2015).
 - [11] A. Omran, M. Boll, T. A. Hilker, K. Kleinlein, G. Salomon, I. Bloch, and C. Gross, *Physical Review Letters* **115**, 263001 (2015).
 - [12] A. Alberti, C. Robens, W. Alt, S. Brakhane, M. Karski, R. Reimann, Artur Widera, and D. Meschede, *New Journal of Physics* **18**, 053010 (2016).
 - [13] J. F. Sherson, C. Weitenberg, M. Endres, M. Cheneau, I. Bloch, and S. Kuhr, *Nature* **467**, 68 (2010).
 - [14] P. Schauss, *High-resolution imaging of ordering in Rydberg many-body systems*, Ph.D. thesis, Ludwig-Maximilians-Universität München (2015).
 - [15] M. Miranda, R. Inoue, Y. Okuyama, A. Nakamoto, and M. Kozuma, *Physical Review A* **91**, 063414 (2015).
 - [16] M. F. Parsons, *Probing the Hubbard Model With Single-Site Resolution*, Ph.D. thesis, Harvard University (2016).
 - [17] L. W. Cheuk, *Quantum Gas Microscopy of Strongly Correlated Fermions*, Ph.D. thesis, Massachusetts Institute of Technology (2017).
 - [18] R. Yamamoto, H. Ozawa, D. C. Nak, I. Nakamura, and T. Fukuhara, *New Journal of Physics* **22**, 123028 (2020).
 - [19] K. Kwon, K. Kim, J. Hur, S. Huh, and J.-y. Choi, *Physical Review A* **105**, 033323 (2022).
 - [20] A. La Rooij, C. Ulm, E. Haller, and S. Kuhr, *New Journal of Physics* **25**, 083036 (2023).
 - [21] J. Mongkolkiattichai, L. Liu, D. Garwood, J. Yang, and P. Schauss, *Physical Review A* **108**, L061301 (2023).
 - [22] S. Buob, J. Höschele, V. Makhalov, A. Rubio-Abadal, and L. Tarruell, *PRX Quantum* **5**, 020316 (2024).

- [23] M. Martinez-Dorantes, W. Alt, J. Gallego, S. Ghosh, L. Ratschbacher, Y. Völzke, and D. Meschede, *Physical Review Letters* **119**, 180503 (2017).
- [24] A. H. Burrell, D. J. Szwer, S. C. Webster, and D. M. Lucas, *Physical Review A* **81**, 040302 (2010).
- [25] L. R. B. Picard, M. J. Mark, F. Ferlaine, and R. v. Bijnen, *Measurement Science and Technology* **31**, 025201 (2019).
- [26] J. Verstraten, K. Dai, M. Dixmieras, B. Peaudecerf, T. d. Jongh, and T. Yefsah, arXiv:2404.05699 [quant-ph].
- [27] A. Impertro, J. F. Wienand, S. Häfele, H. von Raven, S. Hubele, T. Klostermann, C. R. Cabrera, I. Bloch, and M. Aidelsburger, *Communications Physics* **6**, 1 (2023).
- [28] J. Winklmann, A. Alberti, and M. Schulz, in *2024 IEEE International Conference on Quantum Computing and Engineering (QCE)*, Vol. 01 (2024) pp. 1048–1057.
- [29] Available at <https://gitlab.in2p3.fr/gaz-quantiques-lcf/strontium/atom-detection>.
- [30] More elaborate models exist, such as the one recently proposed in [43]. These models are useful to simulate a specific experimental setup, less so to provide ‘prototypical’ test images.
- [31] We have also tested our method using an Airy disk, and found no difference in performance. The Gaussian PSF has the advantage of simplifying the construction of the measurement matrix \mathbf{M} .
- [32] G. Demoment and Y. Goussard, *Inversion within the probabilistic framework*, in *Bayesian Approach to Inverse Problems* (John Wiley & Sons, Ltd, 2008) Chap. 3, pp. 59–78.
- [33] Such solver is available in all standard scientific computing library. In Python one may use the `sparse.linalg.cg` routine from the SciPy library [40].
- [34] The SNR is computed for a patch of 30×30 sites (rather than over the full image) to reduce the computation time of the inverse matrix in Eq. (8).
- [35] The optimal estimates in Fig. 3 were obtained using the known, true imaging parameters, rather than the fully unsupervised procedure described in Appendix B. Indeed, fitting the distribution of estimated brightnesses by a Gaussian mixture using an expectation-maximization algorithm can produce unreliable results in certain edge cases.
- [36] The ordinary least squares estimator, $\mathbf{H}_{\text{OLS}} = (\mathbf{M}^\top \mathbf{M})^{-1} \mathbf{M}^\top$, is ill-conditioned when the PSFs have a significant overlap, meaning that its output is exaggeratedly sensitive to the noise in the image.
- [37] K. B. Petersen and M. S. Pedersen, *The matrix cookbook* (2012), version 20121115.
- [38] F. Pedregosa, G. Varoquaux, A. Gramfort, V. Michel, B. Thirion, O. Grisel, M. Blondel, P. Prettenhofer, R. Weiss, V. Dubourg, J. Vanderplas, A. Passos, D. Cournapeau, M. Brucher, M. Perrot, and E. Duchesnay, *Journal of Machine Learning Research* **12**, 2825 (2011).
- [39] S. van der Walt, J. L. Schönberger, J. Nunez-Iglesias, F. Boulogne, J. D. Warner, N. Yager, E. Gouillart, T. Yu, and the scikit-image contributors, *PeerJ* **2**, e453 (2014-06).
- [40] P. Virtanen, R. Gommers, T. E. Oliphant, M. Haberland, T. Reddy, D. Cournapeau, E. Burovski, P. Peterson, W. Weckesser, J. Bright, S. J. van der Walt, M. Brett, J. Wilson, K. J. Millman, N. Mayorov, A. R. J. Nelson, E. Jones, R. Kern, E. Larson, C. J. Carey, Í. Polat, Y. Feng, E. W. Moore, J. VanderPlas, D. Laxalde, J. Perktold, R. Cimrman, I. Henriksen, E. A. Quintero, C. R. Harris, A. M. Archibald, A. H. Ribeiro, F. Pedregosa, P. van Mulbregt, and SciPy 1.0 Contributors, *Nature Methods* **17**, 261 (2020).
- [41] C. R. Harris, K. J. Millman, S. J. van der Walt, R. Gommers, P. Virtanen, D. Cournapeau, E. Wieser, J. Taylor, S. Berg, N. J. Smith, R. Kern, M. Picus, S. Hoyer, M. H. van Kerkwijk, M. Brett, A. Haldane, J. F. del Río, M. Wiebe, P. Peterson, P. Gérard-Marchant, K. Sheppard, T. Reddy, W. Weckesser, H. Abbasi, C. Gohlke, and T. E. Oliphant, *Nature* **585**, 357 (2020).
- [42] Source code available at <https://gitlab.in2p3.fr/gaz-quantiques-lcf/strontium/atom-detection>.
- [43] J. Winklmann, D. Tsevas, and M. Schulz, in *2023 IEEE International Conference on Quantum Computing and Engineering (QCE)*, Vol. 01 (2023) pp. 1349–1359.